

Can we detect aurora in exoplanets orbiting M dwarfs?

A. A. Vidotto¹, N. Feeney¹, J. H. Groh¹[★]

¹ *School of Physics, Trinity College Dublin, the University of Dublin, Dublin-2, Ireland*

Accepted XXX. Received YYY; in original form ZZZ

ABSTRACT

New instruments and telescopes, such as SPIRou, CARMENES and TESS, will increase manyfold the number of known planets orbiting M dwarfs. To guide future radio observations, we estimate radio emission from known M-dwarf planets using the empirical radiometric prescription derived in the solar system, in which radio emission is powered by the wind of the host star. Using solar-like wind models, we find that the most promising exoplanets for radio detections are GJ 674 b and Proxima b, followed by YZ Cet b, GJ 1214 b, GJ 436 b. These are the systems that are the closest to us (< 10 pc). However, we also show that our radio fluxes are very sensitive to the unknown properties of winds of M dwarfs. So, which types of winds would generate detectable radio emission? In a ‘reverse engineering’ calculation, we show that winds with mass-loss rates $\dot{M} \gtrsim \kappa_{\text{sw}}/u_{\text{sw}}^3$ would drive planetary radio emission detectable with present-day instruments, where u_{sw} is the local stellar wind velocity and κ_{sw} is a constant that depends on the size of the planet, distance and orbital radius. Using observationally-constrained properties of the quiescent winds of GJ 436 and Proxima Cen, we conclude that it is unlikely that GJ 436 b and Proxima b would be detectable with present-day radio instruments, unless the host stars generate episodic coronal mass ejections. GJ 674 b, GJ 876 b and YZ Cet b could present good prospects for radio detection, provided that their host-stars’ winds have $\dot{M}u_{\text{sw}}^3 \gtrsim 1.8 \times 10^{-4} M_{\odot} \text{ yr}^{-1} (\text{km/s})^3$.

Key words: stars: planetary systems – stars: low-mass – stars: winds, outflows – planet-star interactions

1 INTRODUCTION

The search for and characterisation of exoplanets is central to a number of current astrophysical research questions and space exploration. There has been rapid progress in exoplanet detection in recent years, with now over 3,800 confirmed exoplanets on record. The most successful detection methods so far have been the transit and the radial velocity methods. Both of these methods are indirect methods of exoplanet detection, which infer the existence of an exoplanet from the effect it has on the host star.

Exoplanets can be directly detected through imaging. A limitation of such method is the high contrast ratio between the intensity of electromagnetic radiation of the planet and its host star in the visible and infrared ranges; approximately 10^9 in the visible and 10^6 in the infrared (Zarka 2007). However, there may exist a direct detection method in the low frequency radio range, between ten and a few hundred MHz (Grießmeier et al. 2011), given that some planets in the solar system are known to emit radiation within this range. This radiation arises via the interaction between planetary magnetic fields and the solar wind (Desch & Kaiser 1984)

and is known as auroral radio emission. For all magnetised solar system planets, this radiation is only 1 to 2 orders of magnitude less intense than the radiation produced by the Sun in the low frequency radio range (Zarka 2007), thus making it favourable for direct detection. A nearly linear relation between the emitted radio power of these planets and the dissipated kinetic power of the incident solar wind has been observed (Desch & Kaiser 1984) and is known as the ‘radiometric Bode’s law’.

It has been theorised that magnetised exoplanets may emit at radio frequencies, analogously to the solar system planets (e.g., Farrell et al. 1999; Lazio et al. 2004). If the radiometric Bode’s law holds true for exoplanetary systems in a similar way as for the solar system planets, one can use stellar wind models to estimate radio emission from exoplanets. It is expected that hot Jupiters produce radio emission that are many orders of magnitude larger than Jupiter (Grießmeier et al. 2005, 2007; Vidotto et al. 2010a, 2012, but see also Weber et al. 2017; Kavanagh et al. 2019), the strongest emitter in the solar system at radio wavelength. This is because hot Jupiters orbit at regions where the stellar wind has a large ram pressure, which can power stronger planetary radio emissions.

The detection of exoplanetary radio emissions would not

★ E-mail: aline.vidotto@tcd.ie

only be a revolutionary method of exoplanet detection, but also an indicative of the presence of an intrinsic planetary magnetic field. Although some studies have proposed the presence of exoplanetary magnetism to interpret spectroscopic transit observations (e.g., Vidotto et al. 2010b; Llama et al. 2011; Kislyakova et al. 2014), the interpretations are not unique (Vidotto et al. 2015a) and there is still no conclusive detection of an exoplanet magnetic field. Planetary magnetic fields are believed to be one of the key ingredients for determining planetary habitability (e.g. Lammer et al. 2007; McIntyre et al. 2019).

In that regard, M dwarf stars have been the prime targets for detecting terrestrial planets in the habitable zone, which is the region around a star in which a planet could host liquid water on its surface (Kasting et al. 1993). An important issue affecting habitability of M dwarf planets is that their host stars remain active for a long part of their lives (West et al. 2008; Irwin et al. 2011) and have high flare and coronal mass ejections (CME) rates (Davenport et al. 2014; Vida et al. 2016, 2017; Kay et al. 2016). This intense activity could be dangerous for a habitable zone planet, as these planets would receive high dosages of high-energy radiation and intense stellar wind/CME, which could strip away their atmospheres (Lammer et al. 2007; Khodachenko et al. 2007; Scalo et al. 2007; Vidotto et al. 2013). Although intense winds could be dangerous for the survival of planetary atmospheres, intense winds and CMEs would power stronger exoplanetary radio emission, thus allowing one to probe magnetism in exoplanets.

Recently, Burkhart & Loeb (2017) predicted the radio emission of the closest exoplanet to us – Proxima b, which orbits an M dwarf star. They estimate Proxima b has radio emission as high as 1 Jy, in a frequency of 0.02 MHz. Due to its close distance to us, Proxima b is one of the most likely candidates for producing radio emissions that could be detectable from Earth (although, with such predicted frequencies, this would not be observed with ground-based instrumentation). In this work, we estimate the radio emission of exoplanets orbiting M-dwarf stars (for predictions relating to hot Jupiters around solar-type stars see, for example, Grießmeier et al. 2007, 2011). At the time of writing, there are nearly 200 planets orbiting stars in the mass range between 0.1 and 0.5 M_{\odot} . The number of known exoplanets orbiting M dwarfs, including exoplanets in their habitable zones, will increase manyfold, with surveys conducted by, e.g., SPIRou (Cloutier et al. 2018), CARMENES (Quirrenbach et al. 2014) and TESS (Sullivan et al. 2015). Due to detection bias, most of the known M-dwarf planets have small semi-major axis, making them favourable candidates for detecting exoplanetary radio emissions.

This paper is divided as follows. Section 2 presents our candidate selection and Section 3 shows the radio emission model, which is based in the work of Vidotto & Donati (2017). Section 4 shows our results, where we estimate the radio emission of exoplanets using two different approaches. In the first approach (Section 4.1), we use simple stellar wind models to derive radio fluxes, and we demonstrate the large influence that stellar wind models have on the predicted radio emission from exoplanets. Since stellar wind properties of M dwarfs are uncertain, in Section 4.2 we present a second approach based on a ‘reverse engineering’ investigation, in which we derive what are the stellar wind properties that

would power *detectable* radio emission with present-day instrumentation. This is then followed by our discussions (Section 5) and conclusions (Section 6).

2 CANDIDATE SELECTION

We make use of the NASA Exoplanet Archive¹ to select 120 exoplanets (Table 1) that fulfil the following selection criteria.

(i) We select stars in the mass range between 0.1 and 0.5 M_{\odot} . Some of the selected stars do not have quoted errors in their masses (namely, KOI-55, Wolf 1061, GJ 3323, GJ 3341, KOI-55, HD 285968, GJ 674, Ross 458, GJ 273, GJ 3293, GJ 3323). For all the others, the errors quoted in stellar masses are within 25%, with the exception of the following stars: K2-72, Kepler-42, K2-9, BD-08 2823, HD 125595, HIP 57274, HD 99492. For the last three stars, masses are quite uncertain (\sim a factor of 2).

(ii) Kepler’s third law was used to convert from orbital period to semi-major axis in the case of planets without defined semi-major axis values on the catalogue.

(iii) Given that the planetary radius is necessary for the computation of planetary radio power and flux, we use the analytical expression from Seager et al. (2007, see their equation (23)) to derive the radii of planets without quoted radii (mostly planets that are not transiting). These planets are highlighted in Table 1 with an asterisk. This analytical expression offers an estimate of planetary radii and is valid for planets with masses below $\sim 23 M_{\oplus}$. We use the formalism for planets with Fe composition, which gives a *lower limit* on the size of rocky planets (Seager et al. 2007). Since the square of the planet radius R_p enters in the radio power computation, a *lower limit* on R_p produces a conservative estimate for planetary radio power and flux. Assuming a silicate composition (MgSiO_3), for example, would increase the quoted radii of these planets by a factor of 1.29 to 1.35, which would increase our estimated radio power by a factor of up to 1.8. Planets with masses above the $\sim 23 M_{\oplus}$ limit or without quoted masses and radii were not included in our sample.

(iv) Finally, some stars did not have quoted radii in the catalogue. For the following stars, we used the radii quoted in Pasinetti Fracassini et al. (2001): GJ 667 C, GJ 163, GJ 674 and GJ 832.

We note the distinction between the radius of the planet and the radius of its dynamo region. As we show in Section 3, the emitted radio power depends on the size of the planet and on its surface magnetic field strength, which depends upon how deep the dynamo region is within the planet. While the former can be derived from observations (item iii above), the latter depends on models. Recent work has suggested that rocky planets² have magnetic dipole moments similar to that of the Earth or smaller (McIntyre et al. 2019). However, depending on its composition, it is possible instead that terrestrial planets might host a stronger magnetic field than that of the Earth – this has been suggested for K2-229b

¹ <https://exoplanetarchive.ipac.caltech.edu/>

² In our sample, average planetary densities $\langle \rho_p \rangle$ range between 1.5 and 7.5 g cm^{-3} , with the exception of K2-137 b (Table 1).

Table 1. Sample of exoplanets studied in this work. Data are from the NASA Exoplanet Archive for most of the properties. Planets with estimated radii assuming Fe composition are highlighted with an asterisk. See Section 2 for a detailed explanation. The last column is the wind constant κ_{sw} that obeys the relation $\dot{M} \gtrsim \kappa_{\text{sw}}/u_{\text{sw}}^3$, with mass-loss rate \dot{M} given in $M_{\odot} \text{ yr}^{-1}$ and local stellar wind velocity u_{sw} in km/s. This equation provides the minimum mass-loss rates required for a stellar wind to produce detectable radio emission with present-day instruments (> 1 mJy, cf. Section 4.2).

Planet name	M_{\star} (M_{\odot})	R_{\star} (R_{\odot})	d (pc)	M_p (M_{\oplus})	R_p (R_{\oplus})	$\langle \rho_p \rangle$ (g cm^{-3})	P_{orb} (d)	sma (au)	sma (R_{\star})	κ_{sw} ($M_{\odot}/\text{yr (km/s)}^3$)
Proxima b*	0.12	0.14	1.29	1.3	1.3	3.1	11	0.049	74.5	1.56×10^{-5}
GJ 876 d*	0.32	0.30	4.68	6.7	2.1	4.1	1.9	0.021	14.9	7.92×10^{-5}
GJ 674 b*	0.35	0.43	4.55	11	2.3	4.7	4.7	0.039	19.5	1.50×10^{-4}
GJ 436 b	0.47	0.46	9.76	22	4.2	1.7	2.6	0.029	13.6	1.78×10^{-4}
YZ Cet b*	0.13	0.17	3.60	0.75	1.1	3.0	2.0	0.016	19.7	1.82×10^{-4}
GJ 411 b*	0.39	0.39	2.55	3.0	1.7	3.5	13	0.079	43.3	2.34×10^{-4}
YZ Cet c*	0.13	0.17	3.60	0.98	1.2	3.0	3.1	0.021	26.4	2.39×10^{-4}
YZ Cet d*	0.13	0.17	3.60	1.1	1.3	3.1	4.7	0.028	34.9	3.48×10^{-4}
GJ 581 b*	0.31	0.29	6.30	16	2.5	5.2	5.4	0.041	30.1	4.31×10^{-4}
GJ 1214 b	0.15	0.22	12.9	6.3	2.8	1.5	1.6	0.014	13.8	5.96×10^{-4}
Ross 128 b*	0.17	0.20	3.38	1.4	1.3	3.2	9.9	0.050	53.3	6.86×10^{-4}
Wolf 1061 b*	0.29	0.31	4.31	1.9	1.5	3.3	4.9	0.037	26.0	7.23×10^{-4}
GJ 273 c*	0.29	0.29	3.80	1.2	1.3	3.1	4.7	0.036	27.0	7.24×10^{-4}
GJ 3323 b*	0.16	0.12	5.32	2.0	1.5	3.3	5.4	0.033	58.8	1.21×10^{-3}
GJ 273 b*	0.29	0.29	3.80	2.9	1.7	3.5	19	0.091	67.5	1.62×10^{-3}
GJ 687 b*	0.45	0.43	4.55	19	2.7	5.6	38	0.170	85.0	1.74×10^{-3}
Wolf 1061 c*	0.29	0.31	4.31	3.4	1.7	3.6	18	0.089	61.7	2.13×10^{-3}
GJ 581 e*	0.31	0.29	6.30	1.7	1.4	3.2	3.1	0.028	20.9	2.15×10^{-3}
GJ 667 C b*	0.33	0.42	6.80	5.7	2.0	4.0	7.2	0.051	25.8	2.44×10^{-3}
GJ 1265 b*	0.18	0.19	10.3	7.4	2.1	4.2	3.7	0.026	29.4	2.57×10^{-3}
GJ 581 c*	0.31	0.29	6.30	5.5	2.0	4.0	13	0.072	53.4	3.82×10^{-3}
LHS 3844 b	0.15	0.19	14.9	–	1.3	–	0.46	0.006	7.04	4.67×10^{-3}
GJ 3779 b*	0.27	0.28	13.7	8.0	2.2	4.3	3.0	0.026	20.0	7.67×10^{-3}
GJ 832 c*	0.45	0.48	4.97	5.4	2.0	4.0	36	0.163	73.0	7.69×10^{-3}
Kapteyn c*	0.28	0.29	3.93	7.0	2.1	4.2	120	0.311	231	8.39×10^{-3}
GJ 1132 b*	0.18	0.21	12.0	1.7	1.4	3.2	1.6	0.015	15.7	8.62×10^{-3}
GJ 876 e*	0.32	0.30	4.68	15	2.5	5.1	120	0.334	240	9.54×10^{-3}
GJ 625 b*	0.30	0.31	6.49	2.8	1.6	3.5	15	0.078	54.3	1.05×10^{-2}
HD 285968 b*	0.45	0.45	9.47	8.3	2.2	4.4	8.8	0.066	31.5	1.08×10^{-2}
Gl 686 b*	0.42	0.42	8.16	7.1	2.1	4.2	16	0.091	46.6	1.31×10^{-2}
GJ 3323 c*	0.16	0.12	5.32	2.3	1.6	3.4	41	0.126	226	1.54×10^{-2}
GJ 667 C c*	0.33	0.42	6.80	3.8	1.8	3.7	28	0.125	64.0	2.30×10^{-2}
Wolf 1061 d*	0.29	0.31	4.31	7.7	2.1	4.3	220	0.470	326	2.51×10^{-2}
GJ 3634 b*	0.45	0.43	19.8	8.3	2.2	4.4	2.6	0.029	14.3	3.89×10^{-2}
LHS 1140 c	0.18	0.21	12.5	1.8	1.3	4.8	3.8	0.027	27.4	4.54×10^{-2}
GJ 163 b*	0.40	0.44	15.1	11	2.3	4.7	8.6	0.061	29.7	4.66×10^{-2}
GJ 1132 c*	0.18	0.21	12.0	2.6	1.6	3.5	8.9	0.048	48.7	4.92×10^{-2}
GJ 667 C f*	0.33	0.42	6.80	2.5	1.6	3.4	39	0.156	79.8	5.61×10^{-2}
GJ 3998 b*	0.50	0.49	17.8	2.5	1.6	3.4	2.6	0.029	12.7	9.38×10^{-2}
GJ 667 C e*	0.33	0.42	6.80	2.5	1.6	3.4	62	0.213	109	1.05×10^{-1}
LHS 1140 b	0.18	0.21	12.5	7.0	1.7	7.5	25	0.094	95.8	1.67×10^{-1}
K2-25 b	0.29	0.29	45.0	–	3.4	–	3.5	0.030	22.1	1.84×10^{-1}
GJ 4276 b*	0.41	0.41	21.3	17	2.6	5.3	13	0.082	43.0	2.22×10^{-1}
GJ 163 c*	0.40	0.44	15.1	6.8	2.1	4.2	26	0.125	61.3	3.09×10^{-1}
GJ 3998 c*	0.50	0.49	17.8	6.3	2.0	4.1	14	0.089	39.0	3.23×10^{-1}
GJ 667 C g*	0.33	0.42	6.80	4.5	1.9	3.8	260	0.549	281	3.76×10^{-1}
GJ 3341 b*	0.47	0.44	23.2	6.6	2.1	4.1	14	0.089	43.5	8.77×10^{-1}
HIP 57274 b*	0.29	0.78	25.9	6.4	2.0	4.1	8.1	0.070	19.3	8.81×10^{-1}
GJ 3293 e*	0.42	0.40	20.2	3.3	1.7	3.6	13	0.082	44.1	9.11×10^{-1}
HD 85512 b*	0.43	0.71	11.3	3.2	1.7	3.6	58	0.260	78.7	9.20×10^{-1}
K2-18 c*	0.36	0.41	34.0	7.5	2.1	4.3	9.0	0.060	31.5	1.63×10^0
HD 125595 b*	0.29	0.74	28.2	6.4	2.0	4.1	9.7	0.080	23.2	1.63×10^0
K2-28 b	0.26	0.29	63.1	–	2.3	–	2.3	0.021	15.9	1.75×10^0
Kepler-42 c	0.13	0.17	38.7	–	0.73	–	0.45	0.006	7.59	2.00×10^0
GJ 3293 d*	0.42	0.40	20.2	7.6	2.1	4.3	48	0.194	104	2.09×10^0
BD-08 2823 b*	0.50	0.71	41.4	13	2.4	4.9	5.6	0.060	18.2	2.14×10^0
GJ 3293 c*	0.42	0.40	20.2	21	2.7	5.8	120	0.362	194	2.81×10^0
Kepler-42 b	0.13	0.17	38.7	–	0.78	–	1.2	0.012	14.7	5.57×10^0

Table 1 – *continued*

Planet name	M_\star (M_\odot)	R_\star (R_\odot)	d (pc)	M_p (M_\oplus)	R_p (R_\oplus)	$\langle\rho_p\rangle$ (g cm^{-3})	P_{orb} (d)	sma (au)	sma (R_\star)	κ_{sw} ($M_\odot/\text{yr (km/s)}^3$)
K2-18 b	0.36	0.41	34.0	8.9	2.4	3.7	33	0.143	74.9	6.10×10^0
K2-146 b	0.33	0.33	79.5	–	2.2	–	2.6	0.026	16.9	8.74×10^0
K2-129 b	0.36	0.36	27.8	–	1.0	–	8.2	0.057	34.0	1.15×10^1
Kepler-1624 b	0.50	0.47	199	–	5.7	–	3.3	0.034	15.7	1.22×10^1
Kepler-445 c	0.18	0.21	90.0	–	2.5	–	4.9	0.032	32.5	1.25×10^1
HD 99492 b*	0.48	0.83	55.7	22	2.7	5.9	17	0.120	31.1	1.71×10^1
K2-91 b	0.29	0.28	62.7	–	1.1	–	1.4	0.016	12.6	2.00×10^1
Kepler-42 d	0.13	0.17	38.7	–	0.57	–	1.9	0.015	19.5	3.48×10^1
K2-137 b	0.46	0.44	99.1	< 160	0.89	< 1300	0.18	0.006	2.83	3.70×10^1
Kepler-445 b	0.18	0.21	90.0	–	1.6	–	3.0	0.023	23.4	3.97×10^1
K2-151 b	0.47	0.45	69.6	–	1.5	–	3.8	0.037	17.8	4.63×10^1
K2-239 b	0.40	0.36	49.0	–	1.1	–	5.2	0.044	26.3	5.39×10^1
K2-242 b	0.38	0.37	110	–	2.5	–	6.5	0.049	28.7	5.88×10^1
Kepler-446 b	0.22	0.24	120	–	1.5	–	1.6	0.016	14.3	8.16×10^1
K2-124 b	0.39	0.39	140	–	2.9	–	6.4	0.049	27.0	9.19×10^1
K2-9 b	0.30	0.31	83.2	–	2.3	–	18	0.091	63.1	1.08×10^2
K2-45 b	0.50	0.45	502	–	6.7	–	1.7	0.022	10.7	1.10×10^2
Kepler-504 b	0.33	0.33	75.0	–	1.6	–	9.5	0.061	39.6	1.28×10^2
K2-239 d	0.40	0.36	49.0	–	1.1	–	10.	0.069	40.9	1.30×10^2
K2-239 c	0.40	0.36	49.0	–	1.00	–	7.8	0.058	34.4	1.35×10^2
Kepler-1646 b	0.24	0.26	81.0	–	1.2	–	4.5	0.033	27.3	1.43×10^2
K2-95 b	0.44	0.42	181	–	3.9	–	10.	0.070	35.6	1.59×10^2
K2-72 b	0.27	0.33	66.6	–	1.1	–	5.6	0.040	26.1	1.64×10^2
K2-288 B b	0.33	0.32	65.7	–	1.9	–	31	0.164	110	2.66×10^2
Kepler-732 c	0.49	0.46	150	–	1.3	–	0.89	0.014	6.69	2.82×10^2
Kepler-1582 b	0.28	0.30	112	–	1.5	–	4.8	0.037	26.2	2.99×10^2
K2-104 b	0.43	0.49	190	–	2.0	–	2.0	0.023	10.1	3.27×10^2
K2-72 d	0.27	0.33	66.6	–	1.0	–	7.8	0.050	32.6	3.31×10^2
K2-150 b	0.46	0.44	110	–	2.0	–	11	0.073	35.5	3.42×10^2
Kepler-445 d	0.18	0.21	90.0	–	1.2	–	8.2	0.045	45.8	3.98×10^2
Kepler-560 b	0.34	0.33	88.0	–	1.7	–	18	0.095	62.2	4.42×10^2
K2-72 c	0.27	0.33	66.6	–	1.2	–	15	0.078	50.8	4.70×10^2
K2-88 b	0.26	0.26	111	–	1.2	–	4.6	0.035	28.5	5.45×10^2
Kepler-446 d	0.22	0.24	120	–	1.3	–	5.1	0.035	31.6	5.50×10^2
Kepler-1650 b	0.33	0.33	121	–	0.96	–	1.5	0.018	11.7	5.55×10^2
K2-72 e	0.27	0.33	66.6	–	1.3	–	24	0.106	69.0	5.59×10^2
Kepler-446 c	0.22	0.24	120	–	1.1	–	3.0	0.025	22.2	5.64×10^2
K2-71 b	0.48	0.43	154	–	2.2	–	7.0	0.056	27.9	5.71×10^2
K2-89 b	0.35	0.32	86.2	–	0.62	–	1.1	0.015	9.82	5.73×10^2
K2-83 b	0.48	0.42	126	–	1.2	–	2.7	0.030	15.4	6.68×10^2
Kepler-732 b	0.49	0.46	150	–	2.2	–	9.5	0.069	32.3	7.55×10^2
K2-264 b	0.50	0.47	187	–	2.2	–	5.8	0.050	23.0	8.72×10^2
K2-14 b	0.47	0.45	368	–	4.8	–	8.4	0.063	29.9	9.40×10^2
Kepler-1649 b	0.22	0.25	92.4	–	1.1	–	8.7	0.051	44.2	1.01×10^3
K2-125 b	0.49	0.40	125	–	2.2	–	22	0.121	65.0	1.10×10^3
Kepler-1308 b	0.35	0.34	73.0	–	0.52	–	2.1	0.023	14.3	1.44×10^3
K2-83 c	0.48	0.42	126	–	1.5	–	10.0	0.071	36.5	1.87×10^3
Kepler-1124 b	0.35	0.34	177	–	1.3	–	2.9	0.028	17.5	1.98×10^3
K2-264 c	0.50	0.47	187	–	2.7	–	20	0.113	51.6	2.15×10^3
Kepler-296 c	0.50	0.48	226	–	2.0	–	5.8	0.052	23.3	3.13×10^3
Ross 458 c	0.49	0.63	11.5	2000	14	4.3	21000000	1168.000	399000	4.79×10^3
2MASS J02192210-3925225 b	0.11	0.28	39.4	4400	16	5.8	2100000	156.000	120000	6.04×10^3
Kepler-1439 b	0.46	0.43	215	–	1.5	–	8.1	0.061	30.4	1.23×10^4
Kepler-296 d	0.50	0.48	226	–	2.1	–	20	0.118	52.8	1.34×10^4
Kepler-296 b	0.50	0.48	226	–	1.6	–	11	0.079	35.4	1.68×10^4
K2-54 b	0.42	0.38	176	–	1.2	–	9.8	0.067	38.0	1.69×10^4
Kepler-779 b	0.46	0.44	224	–	0.92	–	7.1	0.056	27.3	7.68×10^4
Kepler-296 e	0.50	0.48	226	–	1.5	–	34	0.169	75.7	9.65×10^4
Kepler-296 f	0.50	0.48	226	–	1.8	–	63	0.255	114	1.12×10^5
Kepler-1652 b	0.40	0.38	252	–	1.6	–	38	0.165	93.6	1.17×10^5
KOI-55 c	0.50	0.20	1180	0.67	0.86	5.7	0.34	0.008	8.17	1.41×10^6
KOI-55 b	0.50	0.20	1180	0.45	0.76	5.5	0.24	0.006	6.45	1.45×10^6

(not in our sample), given its Mercury-like composition and large radius (Aitta 2018). Due to our lack of knowledge in planetary field strengths, in this paper, we assume three different planetary magnetic fields: 0.1 G, 1 G and 10 G.

3 MODEL OF PLANETARY RADIO EMISSION

When the stellar wind interacts with a planet’s magnetic field, it flows around the planet, confining the planet’s magnetic field to a cavity surrounding the planet (Chapman & Ferraro 1930). The extension of this cavity, known as the magnetosphere, can be calculated using pressure balance between the total pressure of the stellar wind (p_{sw}) and the planet’s magnetic pressure (p_B). The total pressure of a stellar wind is the sum of its ram, thermal, and magnetic pressures. Only the wind’s ram pressure is taken into account in this work, thus $p_{sw} = \rho_{sw}u^2$, where ρ_{sw} is the mass density of the stellar wind at the orbit of the planet and $\vec{u} = \vec{u}_{sw} - \vec{v}_K$ is the velocity of the stellar wind particles in the reference frame of the planet, with u_{sw} being the velocity of the stellar wind at the orbit of the planet and v_K the Keplerian velocity of the planet (we assume circular orbit for simplicity, as 84% of the planets studied here have orbital eccentricity <0.2). The pressure due to the planet’s intrinsic magnetic field is $p_B = B^2/8\pi$, with B being the planetary magnetic field intensity at a certain radius r_M from the planet, where the interaction with the stellar wind happens. Assuming a dipolar planetary magnetic field, we have that $B = B_p(R_p/r_M)^3$, where B_p is the planet’s surface magnetic field strength at the pole, and R_p is the planet’s radius. From this, we can estimate the magnetopause distance as

$$\frac{r_M}{R_p} = \xi \left(\frac{(B_p/2)^2}{8\pi\rho_{sw}u^2} \right)^{\frac{1}{6}}, \quad (1)$$

where $\xi = 2^{1/3}$ is a numerical factor that corrects for the effects of electrical currents that flow along the magnetopause (Cravens 2004). In cases where the stellar wind ram pressure is too strong for the planet magnetic field to sustain a magnetosphere, Equation (1) gives $r_M < R_p$. In these cases, we set $r_M = R_p$.

To predict the radio power arising from the interaction with a stellar wind, we use the radiometric Bode’s law, i.e., we assume a linear relationship between the emitted radio power of a planet (P_{radio}) and the kinetic power of the incident solar/stellar wind (P_{sw}): $P_{radio} = \eta_K P_{sw}$, where η_K is the efficiency ratio, which has been determined empirically for solar system planets to be 10^{-5} (Zarka 2007). The dissipated kinetic power of the stellar wind as it interacts with a planetary magnetosphere is approximated as the ram pressure of the stellar wind times the cross sectional area of the planetary magnetosphere, at a relative velocity u (Zarka 2007; Vidotto et al. 2012)

$$P_{sw} = \rho_{sw}u^3\pi r_M^2. \quad (2)$$

Thus giving the planet’s radio power as

$$P_{radio} = \eta_K\rho_{sw}u^3\pi r_M^2. \quad (3)$$

Although here we assume that the input power of planetary radio emissions comes from the dissipated kinetic energy of the stellar wind upon interacting with the planet’s magnetosphere (e.g. Lazio et al. 2004), scalings with the Poynting

flux of the stellar wind also exist (Zarka 2007). As we do not have knowledge of the magnetic field strength of the stars in our sample, we opted to use the scaling with the kinetic power of the stellar wind. Radio emission can also be generated in the interaction with CMEs or in Jupiter-Io-like interactions (*unipolar interaction*, Grießmeier et al. 2007). While the former can increase several orders of magnitude the radio power, the latter would likely generate non-detectable emission (Grießmeier et al. 2007). We will come back to the interaction with CMEs in Section 4.2.

Planetary radio emissions are observed to originate from a planet’s auroral regions, which are strongly magnetised annular rings around a planet’s magnetic poles (Siscoe & Chen 1975). The boundary of a planet’s auroral ring is thought to occur approximately where a planet’s closed and open magnetic field lines meet (Hill 2001), and is also referred to as the planet’s polar cap (Tarduno et al. 2010; Vidotto et al. 2013). Planetary aurorae are powered by magnetospheric currents that cause the precipitation of energetic electrons in the polar regions of the upper atmosphere (Wu & Lee 1979; Hallinan et al. 2015), leading to radio emissions via the cyclotron-maser instability mechanism (Zarka 2007). The electrons are theorised to be accelerated along high-latitude field lines due to energy released during magnetic field line reconnection events in the nightside of the planet. In this work, we assume that radio emissions originate from the boundary of open and closed magnetic field lines at the colatitude of the planet’s polar cap, as in Vidotto & Donati (2017). This colatitude (α_0) is related to the planet’s magnetospheric size and radius as (Vidotto et al. 2011a)

$$\alpha_0 = \arcsin \left[\left(\frac{R_p}{r_M} \right)^{1/2} \right] \quad (4)$$

Assuming dipolar magnetic fields, the surface magnetic field strength at this colatitude is given as

$$B(\alpha_0) = \frac{1}{2}B_p[1 + 3\cos^2(\alpha_0)]^{1/2}. \quad (5)$$

When assessing the detectability of exoplanetary radio emissions, one needs to consider their frequency of emission and flux density. Planetary radio emissions are produced at a frequency close to that of the local electron cyclotron frequency. We assume that the emission bandwidth Δf is approximately equal to the electron cyclotron frequency, thus

$$\Omega_{cyc} = \frac{eB}{2\pi m_e c}, \quad (6)$$

where e is the charge of the electron, m_e is the electron mass, and c is the speed of light. Therefore, planets will radiate at a radio frequency determined by the magnetic field strength within the region where electron cyclotron-maser instability can occur. The maximum frequency occurs at the point where the planetary magnetic field is maximum, i.e., near the polar cap regions at the planetary surface. Thus, we have

$$\Delta f = 2.8 \left(\frac{B(\alpha_0)}{1\text{G}} \right) \text{MHz}. \quad (7)$$

Finally, the planetary radio flux density, which is the strength of the signal that is detected on Earth, is

$$\phi_{radio} = \frac{P_{radio}}{d^2\omega\Delta f}, \quad (8)$$

where d is the distance to the system, and ω is the solid angle of the hollow cone of emission (Vidotto & Donati 2017)

$$\omega = 2 \int_{\alpha_0 - \delta\alpha/2}^{\alpha_0 + \delta\alpha/2} \sin \alpha d\alpha d\varphi = 4\pi \left[\cos(\alpha_0 - \frac{\delta\alpha}{2}) - \cos(\alpha_0 + \frac{\delta\alpha}{2}) \right], \quad (9)$$

where the thickness of the cone is $\delta\alpha = 17.5^\circ$ (Zarka et al. 2004). The factor of two in the previous equation accounts for emission coming from both northern and southern hemispheres.

4 ESTIMATING RADIO EMISSION FROM M-DWARF PLANETS

In order to calculate the stellar wind power dissipated in the planet's magnetosphere, we need values of the local density ρ_{sw} and velocity u_{sw} of the stellar wind. Since stellar winds of M dwarfs are poorly constrained, we proceed with two different approaches.

4.1 Approach 1: Using hydrodynamic models of stellar winds

In this first approach, we model the stellar wind as being thermally driven, spherically symmetric and in steady state (Parker 1958). For that, we solve the momentum equation of the stellar wind

$$\rho u \frac{du}{dR} = -\frac{GM_\star}{R^2} - \frac{dp}{dR} \quad (10)$$

where $p = \rho k_B T / \bar{m}$ is the stellar wind thermal pressure, with k_B being the Boltzmann constant, T the isothermal wind temperature and $\bar{m} = 0.5m_p$ is the average mass of the stellar wind particle, taken to be a fully ionised, plasma of hydrogen (whose mass is m_p). The radial distance from the star is taken to be R in Equation (10). Once a solution for the wind velocity $u(R)$ is found, the density profile is found from mass conservation $\rho(R)u(R)R^2 = \text{constant}$. The local conditions for the stellar wind is found then at the semi-major axis of the planet $R = a$, and thus $\rho_{\text{sw}} \equiv \rho(a)$ and $u_{\text{sw}} \equiv u(a)$.

The stellar masses M_\star and radii R_\star were taken from the NASA Exoplanet Archive (see Section 2). An uncertainty in the stellar mass affects the stellar wind profile through the gravity force (second term in equation 10). A variation of $\pm 10\%$ in mass for a $0.5-M_\odot$ star causes a negligible change in the terminal velocity (within $\mp 1\%$). The density profile is more affected though, leading to changes in mass-loss rates of a factor of 0.6 and 1.6 for variations of -10% and $+10\%$ in stellar masses, respectively. However, values of the temperature and base density of stellar winds are the most uncertain in our models. We adopt three different sets of temperature and base density. In our fiducial model (Section 4.1.1), for simplicity, we assume solar values for all the stars in our sample, with a temperature of 1.56×10^6 K, and base number density (electrons and protons) of $2.2 \times 10^8 \text{ cm}^{-3}$ (O Fionnagain & Vidotto 2018). For the second and third models, we vary the temperature and density by factors of 2 (Section 4.1.2).

4.1.1 Fiducial wind model (solar-like wind)

In this subsection, we calculate the planetary radio emission using the fiducial stellar wind model. Our computed radio

power for each planet are shown in Figure 1a, for 1 G (symbols), 0.1 G (lower values of bars), and 10 G (upper values of bars). Our plot shows P_{radio} as a function of semi-major axis, where we see a trend of decreasing P_{radio} with increasing semi-major axis (we normalise the semi-major axis with stellar radius, as this is the relevant distances in stellar wind computations, Vidotto et al. 2013). The spread seen in this correlation is due to the fact that planets are orbiting different stars of varying mass and radius, resulting in different local stellar wind properties, and that each planet has a different size. K2-45b has the strongest radio power of the sample (10^{18} erg/s, for $B_p = 0.1$ G), mostly due to its small semi-major axis ($0.022 \text{ au} \approx 11R_\star$) – planetary radio power is strongest for close-in planets, where the stellar wind ram pressure is higher.

Figure 1b shows our calculated radio flux density for the exoplanets in our sample. Again, these results are for three magnetic field strengths: 1 G (symbols), 0.1 G (upper values of bars), and 10 G (lower values of bars). For these magnetic field strengths, emissions would occur at a maximum frequency of approximately 2.5, 0.22 and 27 MHz, respectively, averaged among the planets in our sample. Though K2-45b has the highest radio power of all of the planets, it has a very low flux density of $0.07 \mu\text{Jy}$, for a 0.1G field. GJ 674 b and Proxima b have the highest flux density of 200 and $180 \mu\text{Jy}$, respectively, followed by YZ Cet b, GJ 1214 b, GJ 436 b with flux densities around $83 \mu\text{Jy}$, for a 0.1G field. K2-45b and some of these planets are highlighted in Figure 1. From the right panel, there is no clear correlation (i.e., large spread) between radio flux density and semi-major axis, that was seen in the plot of radio power (left panel). This increased spread is due to the variety of distances to the systems (depicted in the colours of the symbols). An increased magnetic field strength results in a small decrease in flux density, in spite of an increase seen in P_{radio} . For example, in the case of Proxima b, increasing the dipolar field from 1 G to 10 G, results in a flux that is a factor of 1.5 smaller. In our sample, a 2-order-of-magnitude increase in B_p from 0.1 G to 10 G causes a decrease in radio fluxes by only a factor of 2.2 to 5.2, with an average of ~ 2.7 . For the 1-G case, solid angles range from 0.4 to 2.8 sr, with a peak distribution at 1.7 sr, similar to the Jovian value of ~ 1.6 sr (Zarka et al. 2004).

The symbol colours shown in Figure 1b depict distance to the system, with green representing objects that are closer to us, within 5 pc, and red representing objects at a distance between 5 and 10 pc, and blue between 10 and 50 pc. For reference, the expected value of Jupiter's emission, if Jupiter were at a distance of 50 pc, is at around $1 \mu\text{Jy}$ (Bastian et al. 2000). For $B_p = 0.1$ G, the flux densities range from 10^{-6} to $200 \mu\text{Jy}$. There is a tight negative correlation between flux and distance due to the inverse square relationship between the two (Equation 8), which explains why the green and red symbols are all at the upper part of Figure 1b, with the more distant systems (empty symbols) at the bottom part. The top-4 exoplanets with the strongest flux densities (Proxima b, GJ 674 b, GJ 436 b, YZ Cet b) orbit some of the closest known M-dwarf planetary systems (1.3, 4.55, 9.76 and 3.6pc, respectively). In contrast, K2-45b, which has the highest radio power, is more than 500 pc away, thus explaining its low flux density.

The second largest radio flux density among the planets in our study is that of Proxima b. Given that Proxima b is

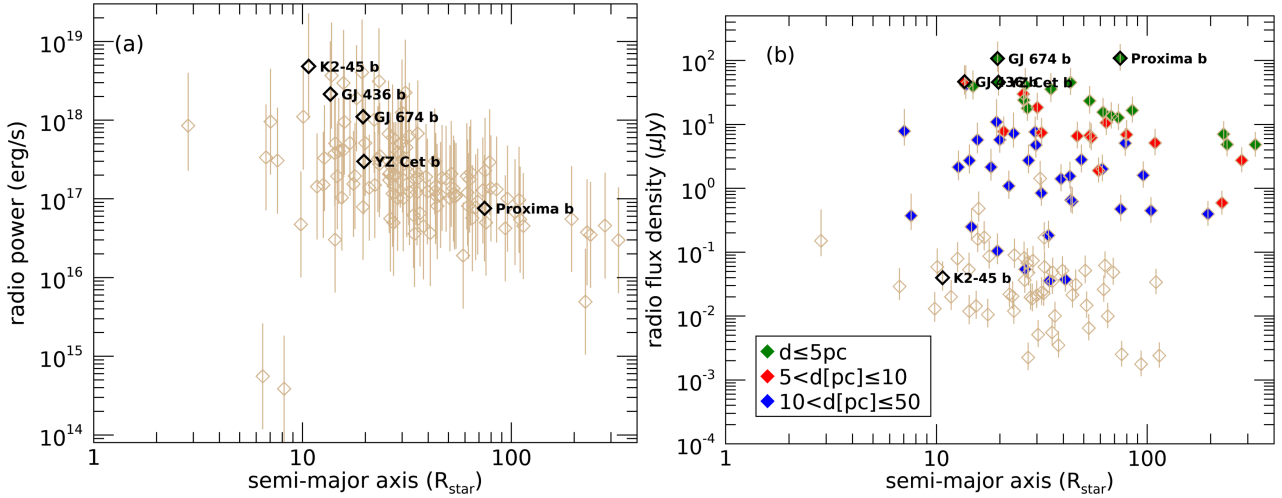


Figure 1. Radio power (a) and radio flux densities (b) of exoplanets listed in Table 1. The symbols represent a magnetic field strength of 1G, with the bars representing calculations done for 0.1G and 1G. The corresponding frequencies of emission are 2.5, 0.22 and 27 MHz, respectively. The values shown here are very sensitive to assumptions of stellar wind models. A model that is independent of the stellar wind driving mechanism is presented in Section 4.2. Distance is depicted as symbol colour in panel b.

an Earth-sized planet, Zuluaga & Bustamante (2016) estimated its magnetic field to be in the range of 0.1 to 0.3 G. From our models with $B_p = 0.1$ G, we found a flux density of $180 \mu\text{Jy}$. Recently, Burkhardt & Loeb (2017) predicted Proxima b can emit between a few mJy up to 1 Jy depending on the assumed magnetic field of the planet (from 1G to 0.007G, respectively, cf. their Figure 3, lower panel). For a magnetic field of 0.1G, they predicted emission on the range of 4 to 30 mJy or even one order of magnitude higher if the dissipated power comes from the Poynting flux of the stellar wind. Our value ($180 \mu\text{Jy}$) differs from the ones (4 to 30 mJy) derived by Burkhardt & Loeb (2017) by one to two orders of magnitude. We attribute this disagreement to differences in the models – for example, the frequency bandwidth in our model depends on the local value of the planetary surface field at the polar cap, while in Burkhardt & Loeb (2017)’s model, it depends on the polar strength of the dipole. However, we believe that the main reason for the disagreement in radio flux lies in the local condition of the stellar wind, which they assume to have a velocity of 1600 km/s (nearly 3 times faster than ours) and a density of about 1000 protons/cm⁻³ (twice larger than ours). We investigate the influence of the stellar wind properties on planetary radio emission next.

4.1.2 Influence of the stellar wind properties

Unfortunately, the values of the local stellar wind density ρ_{sw} and velocity u_{sw} are difficult to derive from observations. This is because the hot winds of cool dwarf stars are difficult to detect (Wood 2004). In particular for M dwarfs, there is currently only few observational constraints, such as for Proxima Cen (Wood et al. 2001), EV Lac (Wood et al. 2005), GJ 436 (Vidotto & Bourrier 2017), V374 Peg and HK Aqr (Jardine & Collier Cameron 2019) and, so far, considerably fewer models of winds of M dwarfs (Vidotto et al. 2011b, 2014; Garraffo et al. 2016; Vidotto & Bourrier 2017; Jardine & Collier Cameron 2019) than those proposed for sun-like stars.

To quantify how the stellar wind affects radio flux densities, we perform the radio calculations for two additional wind models. Our original model assumes a wind temperature of $T \equiv T_{\odot} = 1.56 \times 10^6$ K, and base number density of $n \equiv n_{\odot} = 2.2 \times 10^8$ cm⁻³. These values are typical of the solar wind. A second wind model has a temperature of 3.12×10^6 K, twice as large, and the same base density of 2.2×10^8 cm⁻³. Finally, a third model has the same temperature as the second one, but with a twice as large base density of 4.4×10^8 cm⁻³. We refer to each of these models as $\{T_{\odot}, n_{\odot}\}$, $\{2T_{\odot}, n_{\odot}\}$ and $\{2T_{\odot}, 2n_{\odot}\}$, respectively.

The velocity of an isothermal wind is rather sensitive to temperature, but is independent of the choice of base density. This means that the stellar wind velocity at the planetary orbit is higher in model $\{2T_{\odot}, n_{\odot}\}$ than in model $\{T_{\odot}, n_{\odot}\}$. Because the velocity profile changes (more accelerated in model $\{2T_{\odot}, n_{\odot}\}$), the density structure also changes, seeing a slower decay with distance in the hotter of the two models. This also translates to a higher mass loss rate for the hotter model. The radial velocity profile of the stellar wind for models $\{2T_{\odot}, n_{\odot}\}$ and $\{2T_{\odot}, 2n_{\odot}\}$ are the same, but the local wind densities are a factor of 2 higher in the model $\{2T_{\odot}, 2n_{\odot}\}$. In our sample, local velocities for models $\{2T_{\odot}, n_{\odot}\}$ and $\{2T_{\odot}, 2n_{\odot}\}$ are on average 1.7 times larger than for model $\{T_{\odot}, n_{\odot}\}$, ranging between factors of 1.5 and 2.9. Local densities are a factor 32 larger, on average, for model $\{2T_{\odot}, n_{\odot}\}$ compared to $\{T_{\odot}, n_{\odot}\}$ (the factor ranges from 2.8 to 1500). Mass-loss rates are on average a factor of 78 larger for $\{2T_{\odot}, n_{\odot}\}$ than for $\{T_{\odot}, n_{\odot}\}$ (factors ranging from 4.4 up to 3700), and then again a factor of 2 larger for $\{2T_{\odot}, 2n_{\odot}\}$ compared to $\{2T_{\odot}, n_{\odot}\}$.

Overall, the stellar wind model $\{2T_{\odot}, 2n_{\odot}\}$ presents the highest ram pressure as both the local wind density ρ_{sw} and velocity u_{sw} are the largest of all the three models. This has two counter effects in planetary radio emission. While the radio power depends on the ram pressure (Equation 3), it also depends on the area of the planetary magnetosphere, which decreases for higher ram pressure (Equation 1). Math-

ematically, we have that $P_{\text{radio}} \propto \rho_{\text{sw}} u^3 r_M^2 \propto \rho_{\text{sw}} u^3 / (\rho_{\text{sw}} u^2)^{1/3} \propto (\rho_{\text{sw}} u^2)^{2/3} u$. Hence, we expect that the hotter (i.e., higher velocities u_{sw} and thus higher relative velocities $u = (u_{\text{sw}}^2 + v_K^2)^{1/2}$) and the denser the wind is, the dissipated radio power will be higher. The dependence of the radio flux with the density and velocity is slightly more complicated (Equation 8), as we also need to consider the other two factors in the denominator, ω and Δf , which depend on the colatitude of the polar cap α_0 . In the limiting case of a radio emission that is powered by the kinetic energy of the stellar wind, we can write that $\phi_{\text{radio}} \propto \rho_{\text{sw}}^{1/2} u^2 f(\alpha_0)$ (Equation B.1 in Vidotto & Donati 2017). The function $f(\alpha_0)$ ranges between ~ 0 and 3.3, for any given value of α_0 between ~ 0 (small polar cap) and 90 degrees (crushed magnetosphere in the surface of the planet), respectively. Thus, the denser and hotter the wind is, the smaller the magnetosphere and hence the larger the value of $f(\alpha_0)$. Altogether, this leads to larger values of ϕ_{radio} .

This can indeed be seen in Figure 2a, where we present the radio flux densities of the exoplanets in our sample for the three different wind models. For this calculation, we keep the value of the planetary dipolar field strength fixed to $B_p = 0.1$ G. The stellar wind model $\{2T_\odot, 2n_\odot\}$ induces the highest radio emission for all planets, followed by model $\{2T_\odot, n_\odot\}$ and our typical solar wind value case (model $\{T_\odot, n_\odot\}$) leading to the smallest radio flux among all the three stellar wind models. We note the distance-squared decay of the radio flux very clearly in this figure – the outlier point at 11.5pc, with low flux density, is Ross 458c, which has one of the largest semi-major axis in our sample (i.e., with weak stellar wind). Figure 2b shows the ratio of radio fluxes predicted with model $\{2T_\odot, 2n_\odot\}$ over those of model $\{T_\odot, n_\odot\}$. Overall, the discrepancy between the two computed fluxes are factors between ~ 10 and 60, but reaches above 200 for two exoplanets seen in the figure. The discrepancy is larger for close-in planets, which is also the region favoured in the detection of exoplanets, due to detection bias.

In the case of Proxima b, for example, the radio flux density increases from 0.18mJy for model $\{T_\odot, n_\odot\}$ to 1.6mJy for model $\{2T_\odot, n_\odot\}$ to 2.6mJy for model $\{2T_\odot, 2n_\odot\}$. Our model $\{2T_\odot, 2n_\odot\}$ produces a local wind velocity of 885 km/s and proton density of about 5600 protons/cm⁻³, which is approximately factors of 1/2 and 5, respectively, compared to the values adopted in Burkhardt & Loeb (2017). This explains why only model $\{2T_\odot, 2n_\odot\}$ has a radio flux for Proxima b that is more similar to the ones derived in Burkhardt & Loeb (2017). The most promising target, GJ 674 b, sees an increase in the radio flux density from 0.2mJy to 4.6mJy by changing the density and temperature of the stellar wind model by factors of 2.

4.2 Approach 2: Deriving local properties of stellar winds that power detectable radio emission

As demonstrated in Figure 2, an uncertainty in the wind properties of M-dwarf stars can generate a significant uncertainty in the predicted radio emission. Which type of stellar wind would generate detectable radio emission? Before we present the results of our computation, we stress that, contrary to the results presented in Section 4.1, the stellar winds we discuss in this section do not depend on any particular wind model. Rather, the results shown next only depend on

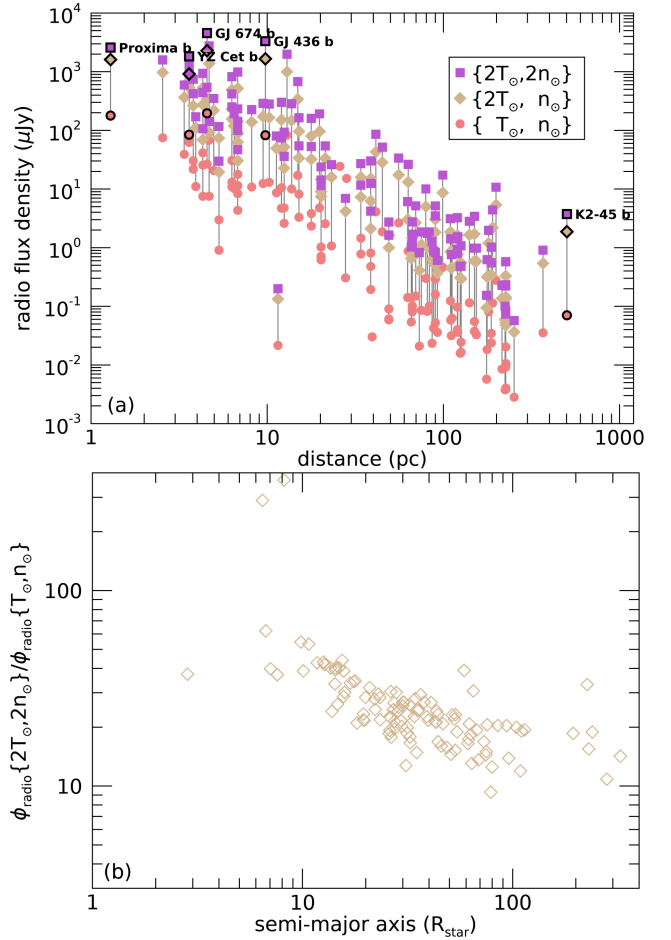


Figure 2. (a) Radio flux density predictions assuming a planetary dipolar field strength of 0.1 G and their dependence on distance to the system. Three stellar wind conditions are investigated, ranging from typical base values of the solar wind and twice its temperature and density. Hotter and denser winds induce overall higher planetary radio emissions. (b) Ratio between the radio flux density derived with model $\{2T_\odot, 2n_\odot\}$ and $\{T_\odot, n_\odot\}$ as a function of orbital distance. Uncertainties in the stellar wind properties affect more the radio predictions of close-in planets.

the local property of the stellar wind at the orbit of planets and not on which physical mechanism is responsible for accelerating the winds to such velocities.

In the limiting case of a radio emission that is powered by the kinetic energy of the stellar wind, we have (Equation B.1 in Vidotto & Donati 2017)

$$\phi_{\text{radio}} = \eta'_K \frac{R_p^2}{d^2} \rho_{\text{sw}}^{1/2} u^2 f(\alpha_0), \quad (11)$$

where $\eta'_K \simeq \eta_K 1.8 \times 10^{-8} = 1.8 \times 10^{-13}$ (in cgs units), $u = (u_{\text{sw}}^2 + v_K^2)^{1/2}$ is the relative velocity and

$$f(\alpha_0) = \frac{\sin^2 \alpha_0}{[\cos(\alpha_0 - \delta\alpha/2) - \cos(\alpha_0 + \delta\alpha/2)](1 + 3 \cos^2 \alpha_0)^{1/2}}, \quad (12)$$

where we note that $0 \lesssim f(\alpha_0) < 3.3$. Note that our ignorance on B_p is hidden in the function $f(\alpha_0)$, through Equations (1)

and (4). Rewriting Equation (11), we have

$$\rho_{\text{sw}}^{1/2} u^2 = \frac{\phi_{\text{radio}}}{\eta_K} \frac{d^2}{R_p^2} \frac{1}{f(\alpha_0)}. \quad (13)$$

Let us assume now that $f(\alpha_0)$ takes its *largest* value of ≈ 3.3 . In this case, we estimate that the *minimum* required property of the local stellar wind is

$$\left\{ \left(\frac{n_{p,\text{sw}}}{1 \text{ cm}^{-3}} \right)^{1/2} \left(\frac{u}{1 \text{ km/s}} \right)^2 \right\}_{\text{min}} \approx \frac{\phi_{\text{radio}}/(1 \text{ mJy})}{7.6 \times 10^{11}} \left(\frac{d}{R_p} \right)^2, \quad (14)$$

where we converted the total mass density in proton density ($\rho_{\text{sw}} = n_{p,\text{sw}} m_p$). Alternatively, we can rewrite Equation (14) in terms of mass-loss rates \dot{M}

$$\left\{ \left(\frac{\dot{M}}{M_{\odot} \text{ yr}^{-1}} \right)^{1/2} \left(\frac{u}{1 \text{ km/s}} \right)^{3/2} \right\}_{\text{min}} \approx \frac{\phi_{\text{radio}}/(1 \text{ mJy})}{2.8 \times 10^{20}} \left(\frac{d}{R_p} \right)^2 \frac{a}{1 \text{ au}}, \quad (15)$$

where we used $\dot{M} = \rho_{\text{sw}} u_{\text{sw}} 4\pi a^2$, for a spherically symmetric stellar wind. Equations (14) and (15) imply that, in case of radio detection, we cannot decouple the local density (or mass-loss rate) from the local velocity of the stellar wind, unless we provide additional hypotheses (or additional observations).

The curves in Figure 3 (Equations (14) and (15) in the top and bottom panels, respectively) show the dependences of the stellar wind properties for a given radio flux density of 1 mJy. We chose this (optimistic) value of radio flux as this would generate detectable radio emission (i.e., above instrument sensitivity limit) for present-day instruments (Section 5). If the sensitivity limit becomes lower, then the curves in Figure 3 would shift down, i.e., the minimum required wind properties become smaller. We only show the curves for some selected systems, for which the right-hand side of Equation (14) provides the minimum values in our sample (i.e., systems that have the smallest values of d/R_p in the sample). The inflexion seen in some of the curves towards low stellar wind velocities is because Equations (14) and (15) are written with respect to relative velocity u while the curves are plotted against u_{sw} . The several points shown in Figure 3 are constraints derived from observations and will be described in Section 4.2.1.

Table 1 shows, for all the exoplanets in our sample, the wind constant κ_{sw} that obeys the relation

$$\dot{M} \gtrsim \kappa_{\text{sw}} / u_{\text{sw}}^3, \quad (16)$$

with mass-loss rate \dot{M} given in $M_{\odot} \text{ yr}^{-1}$ and local stellar wind velocity u_{sw} in km/s, where

$$\kappa_{\text{sw}} = \left[\frac{\phi_{\text{radio}}/(1 \text{ mJy})}{2.8 \times 10^{20}} \left(\frac{d}{R_p} \right)^2 \frac{a}{1 \text{ au}} \right]^2 \quad (17)$$

(cf. Equation 15). These equations provide the minimum mass-loss rates required for a stellar wind to power a given radio flux ϕ_{radio} . The best candidates for radio detection among the planets in our sample are Proxima b, GJ 436 b, GJ 674 b, GJ 876 b and YZ Cet b. To be detected with current instrumentation, the quiescent winds of their hosts should have $\dot{M} u_{\text{sw}}^3 \gtrsim 1.8 \times 10^{-4} M_{\odot} \text{ yr}^{-1} (\text{km/s})^3$. As we will see next, the quiescent winds of some of these stars are likely too weak to power detectable radio emission.

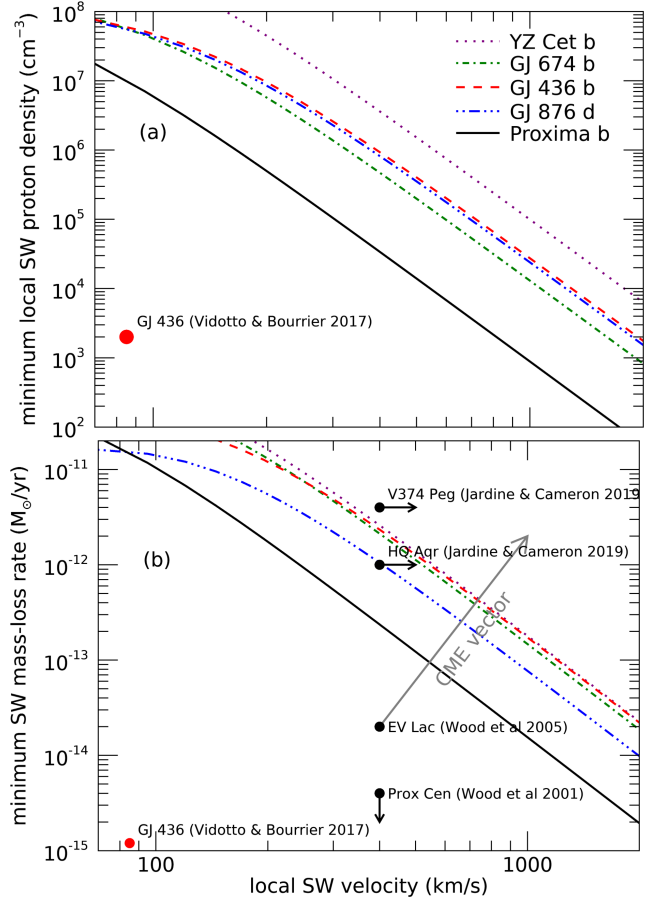


Figure 3. Minimum stellar wind properties required to generate a radio flux density of 1 mJy for selected exoplanets. (a) Minimum local density of the stellar wind and (b) Minimum mass-loss rate as a function of the local stellar wind velocity. Contrary to Figure 1, these plots do not depend on stellar wind models (i.e., their mechanism of acceleration), but rather only on the local conditions of the stellar wind. Some M dwarfs with observational constraints for their stellar winds are shown. Coronal mass ejections are expected to increase velocities and mass-loss rates, which would momentarily power radio emission to detectable levels.

4.2.1 Observational constraints of M dwarf winds

In order to assess the observability of radio emission from M dwarf exoplanets we add some available observational constraints of the winds of M dwarfs to Figure 3 – these are represented by filled circles. Values of mass-loss rates and wind velocities³ are quoted for Proxima Cen (Wood et al. 2001), EV Lac (Wood et al. 2005), GJ 436 (Vidotto & Bourrier 2017), V374 Peg and HK Aqr (Jardine & Collier Cameron 2019). For the last two objects, we assume a (terminal) velocity of ~ 400 km/s but note that for active M dwarfs, these values are likely higher (Vidotto et al. 2011b; Villarreal D’Angelo et al. 2018). Of these five objects, only two

³ The quoted velocities are terminal stellar wind velocities, except for GJ436, which we use the local velocity from Vidotto & Bourrier (2017). Note that the solar wind values at 1au match values derived for EV Lac (Wood et al. 2005).

have detected exoplanets and we explore them in more details next.

Assuming a threshold of 1mJy, which is achievable with present-day instruments, we have that, for Proxima b to have a detectable radio emission, the stellar wind should have a minimum mass-loss rate of

$$\dot{M} \gtrsim 1.6 \times 10^{-5} / u_{\text{sw}}^3 \quad \text{for Proxima b.} \quad (18)$$

Note that the typical values used in [Burkhart & Loeb \(2017\)](#) for density (1000 cm^{-3}) and velocity (1600 km/s) are indeed above our minimum line for Proxima b (Figure 3a), confirming the need of relatively high densities and velocities for a detectable radio emission from Proxima b. [Wood et al. \(2001\)](#) derived a mass-loss rate of $< 2 \times 10^{-15} M_{\odot} \text{ yr}^{-1}$ with a terminal velocity of 400 km/s for a quiescent wind of Proxima Cen. These values are below the minimum stellar wind properties, as can be seen in Figure 3b, which implies that such a quiescent wind would not drive radio emission above 1mJy level.

In the case of GJ 436 b, the required host star mass-loss rate is

$$\dot{M} \gtrsim 1.8 \times 10^{-4} / u_{\text{sw}}^3 \quad \text{for GJ 436 b,} \quad (19)$$

(we here assumed that $u \simeq u_{\text{sw}}$). The red circles in Figure 3 show the mass-loss rate, local proton density and stellar wind velocity derived for GJ 436 ([Vidotto & Bourrier 2017](#)). Given these values, it is unlikely that radio emission from GJ 436 b would be detectable with present-day instruments.

Both the quoted values of Proxima Cen and GJ 436 are representative of quiescent winds. However, the passing of a CME would increase the density and velocity of local stellar winds. In the Sun, CMEs can reach velocities above 1000 km/s (e.g. [Gallagher et al. 2003](#)). [Osten & Wolk \(2015\)](#) estimate that CMEs in EV Lac could change the mass-loss rate by 2 orders of magnitude the values derived from [Wood et al. \(2005\)](#). We add therefore a ‘‘CME vector’’ to Figure 3b to indicate the general trend one would expect to achieve with episodic mass ejections. This means that, although quiescent stellar winds might not drive detectable planetary radio emissions, the increase in velocities and densities of CMEs might be able to reach values above our minimum thresholds in Figure 3b.

5 DISCUSSION

Detection of exoplanetary radio emission could help derive stellar wind properties. In this case, the detection frequency would allow one to assess the planetary magnetic field. The radio flux density, on the other hand, would then allow one to derive the stellar wind conditions. Given that the radio flux density is rather sensitive to stellar wind conditions (Figure 2a), radio detection could help us pinpoint the most likely stellar wind properties (Figure 3).

5.1 Ground-based detectability of predicted emissions

One of the key factors in the detection of radio emission from exoplanets is the frequency of emission. Since emission happens at the cyclotron frequency, knowing the magnetic field strength of the planet is a key element to help

guide searches. Our models predict a maximum emission bandwidth of 2.7 MHz for $B_p = 1 \text{ G}$. However, the Earth’s ionosphere reflects electromagnetic radiation of frequencies below 10 MHz, therefore ground-based radio telescopes can not detect signals below this frequency. When the planetary magnetic field strength is increased to 10 G, the maximum emission bandwidth increases to 27 MHz, which is above the Earth’s ionospheric cutoff. There are a number of radio arrays operating in the low frequency range (below $\sim 100 \text{ MHz}$), such as the upgraded Ukrainian T-shaped Radio telescope (UTR-2), the Low-Frequency Array (LOFAR), the Murchison Widefield Array (MWA) and the Owens Valley Long Wavelength Array (OVRO-LWA). Currently, LOFAR offers the best frequency of operation-sensitivity combination: [de Gasperin et al. \(2019\)](#) estimate a sensitivity of about 3mJy/beam at 54MHz, or $\sim 10 \text{ mJy}$ for a 3σ detection. For a 1-h integration time at 20 to 40 MHz, [Griessmeier et al. \(2011\)](#) project a more optimistic sensitivity of about 3 to 30 mJy. The square kilometre array (SKA) will outperform LOFAR in sensitivity, however it is set to operate at frequencies above 50 MHz ([Dewdney et al. 2009](#); [Griessmeier 2017](#)). For a planet to emit at a frequency of over 50 MHz, it would require a minimum magnetic field strength of $\sim 18\text{G}$.

Knowledge of the magnetic fields of exoplanets is currently based on theoretical estimations and extrapolations of solar system models (e.g., [Christensen et al. 2009](#); [Zuluaga & Cuartas 2012](#); [Gastine et al. 2012](#); [Zuluaga & Bustamante 2016](#)). Although some works have suggested means to derive planetary field strengths (e.g. [Vidotto et al. 2010b](#); [Kislyakova et al. 2014](#)), there is still no definitive detection of exoplanetary magnetic fields. Recent studies suggest, however, that rocky planets, such as most of the planets in our sample, would have magnetic dipole moments that are at the most similar to that of the Earth ([McIntyre et al. 2019](#), but see also [Aitta 2018](#) for terrestrial exoplanets with higher predicted magnetic fields). Therefore, if M-dwarf planets have magnetic field strengths $\lesssim 4\text{G}$, as is likely the case of Proxima b ([Zuluaga & Bustamante 2016](#)), radio emissions are not detectable from ground-based radio telescopes. In recent years, there has been discussion of construction of a radio array on the moon ([Lazio et al. 2011](#); [Zarka et al. 2012](#)). Although perhaps not suitable for exoplanet radio emission detection, the Chang’e 4 lander carried a radio astronomy payload, and the Chang’e 4 orbiter carries the Netherlands-Chinese Low-frequency Explorer payload, which may represent first steps towards future radio detection of exoplanets. Similarly, the Sun Radio Interferometer Space Experiment (SunRISE) concept may also present a path forward in future low-frequency space-based radio observatories. Space-based radio instruments would have an enormous impact on the search for exoplanetary radio emissions, allowing signals from low frequency sources, such as exoplanets, to be detected and characterised. The results found in this study, among many others, provide additional motivation for the building of a lunar array.

5.2 Time-dependence of radio emissions

The predictions made here do not take into account potential variability of radio emission. A planet’s magnetosphere, for example, would vary in size due to the changing properties

of stellar winds. Jovian emissions are sporadic at times with transient periods of high-intensity emissions, which correspond to solar flares or coronal mass ejections (Farrell et al. 1999). Proxima Centauri, for example, is expected to have a highly variable stellar wind with frequent flaring events (Davenport et al. 2016). This could mean that radio emissions from Proxima b could vary in intensity, with periods of extremely intense radio emissions that could lie within the ground-based detectable range (Burkhart & Loeb 2017). Rotation of planets can also cause changes in planetary radio emission. For example, for the giant planets of the solar system, the observed flux densities of emission are modulated at the planetary rotation period. This modulation is caused by an offset between their magnetic and rotation axes (Bastian et al. 2000; Zarka 2007). It remains to be seen whether such offsets would exist in exoplanets, and/or if they are sufficiently large to cause a detectable variation in the intensity of radio emissions (Varela et al. 2018).

In addition to short-term variability of planetary radio emission, caused by short-term variability in stellar winds (e.g., due to passing of a CME, Figure 3b), longer term changes in radio emission are also expected (Vidotto et al. 2011c). For example, on scales of days to years, as the planet moves along its orbit, the local properties of stellar winds change. In all the wind models we presented here, the winds are assumed to be spherically symmetric. However, the complex geometries seen in stellar magnetism imply that stellar winds are not homogeneous (Llama et al. 2013; Vidotto et al. 2015b; Alvarado-Gómez et al. 2016; Burkhart & Loeb 2017). On scales of years to decades, we also observe changes in stellar magnetism associated to cycles (Boro Saikia et al. 2016; Mengel et al. 2016; See et al. 2016), which means that stellar winds would also evolve in these timescales (Pinto et al. 2011; Nicholson et al. 2016; Finley et al. 2019). Finally, on evolutionary timescales of Gyr, winds are believed to become more rarefied as the star evolves in the main sequence (See et al. 2014; Johnstone et al. 2015; Gallet & Bouvier 2015; Matt et al. 2015; Ó Fionnagáin et al. 2019).

6 CONCLUSIONS

This work investigated the detectability of radio emission for currently known exoplanets orbiting M dwarf stars. After filtering for planets with host stars in the mass range between 0.1 and 0.5 M_{\odot} , our sample contained 120 exoplanets orbiting M dwarf stars (Table 1). The radio emission calculation was based on the radiometric Bode’s law – an empirical law determined for the solar system, which has since been extrapolated to extrasolar systems. The radiometric Bode’s law depends on the local properties of the host-star wind. In the case of M dwarfs, these properties are still very poorly constrained, both from modelling and observational aspects. We therefore tackled this with two approaches.

In the first approach, we used the host-stars characteristics to construct simple stellar wind models, extracted the wind properties at the orbits of our planets and calculated the radio flux densities of the exoplanets in our sample. Most previous work in this area have focused on hot Jupiters orbiting F, G and K type stars, therefore our study filled the gap by estimating auroral emission from planets orbiting M dwarfs. We assumed these planets have dipolar fields and

adopted three dipolar field strengths: 0.1 G, 1 G and 10 G. Given that the radio emission occurs at the cyclotron frequency, emissions would occur at a maximum frequency of approximately 0.22, 2.5 and 27 MHz (averaged for all the planets in the sample), respectively. Recent works have suggested that rocky planets, as most of the planets in our sample, are more likely to present magnetic moment similar to or smaller than that of the Earth (the Earth’s dipolar field strength at poles is 0.3 G), so the lower magnetic field values of 0.1 and 1 G are preferred. Nevertheless, we showed that there is a weak dependence of the planet’s radio flux density on its magnetic field strength, with a factor of 100 increase in magnetic field strength (from 0.1 to 10 G) resulting in a decrease in flux density by a factor of ~ 2.7 only.

In our sample, K2-45b has the largest radio power due to its large size. However, its estimated flux density is quite small, $< 10 \mu\text{Jy}$, due to it being at a distance of more than 500 pc from us. GJ 674 b, Proxima b, GJ 1214 b, GJ 436 b and YZ Cet b have the strongest flux densities despite their relatively low radio power. Using our simple stellar wind models, we predict flux densities for these exoplanets that are above the mJy level. The higher fluxes are due to their proximity to us as they all orbit stars less than 10 pc from us. Exoplanets of close proximity should be therefore the strongest candidates for future searches of detectable planetary radio emissions. Proxima b is of particular interest due to its proximity (1.3 pc). Given its terrestrial size, dynamo models suggest a magnetic field strength < 1 G. If this is indeed the case, its emission frequency would be below the Earth’s ionospheric cutoff point of 10 MHz and would not be possible to detect Proxima b’s radio emission with ground-based observations.

We demonstrated that the uncertain stellar wind properties of M dwarf stars can generate a significant uncertainty in the predicted radio emission. Although this might seem disappointing at first, we argued that detection of radio emission from exoplanets could help us pinpoint the most likely wind properties of M dwarfs, which are currently very poorly constrained by observations. Therefore, in our second approach, instead of basing radio estimates on unknown properties of stellar winds, we investigated which physical characteristics of the host-star wind are required in order for radio emission to be detectable with present-day instruments at the 1mJy level. We found that the minimum mass-loss rates obey the relation $\dot{M} \gtrsim \kappa_{\text{sw}}/u_{\text{sw}}^3$, with mass-loss rate \dot{M} given in $M_{\odot} \text{ yr}^{-1}$ and local stellar wind velocity u_{sw} in km/s. The derived values of κ_{sw} , calculated assuming a sensitivity limit of 1mJy, are presented in Table 1. For Proxima b, we found that $\dot{M} \gtrsim 1.6 \times 10^{-5}/u_{\text{sw}}^3$ and for GJ 436 b, $\dot{M} \gtrsim 1.8 \times 10^{-4}/u_{\text{sw}}^3$. Given that the quiescent wind values of GJ 436 and Proxima Cen derived in Vidotto & Bourrier (2017) and Wood et al. (2001) are below our minimum \dot{M} limit, it is unlikely that radio emission from GJ 436 b and Proxima b would be detectable with present-day instruments. Detectable emission from these planets could be generated if, for example, these planets interact with coronal mass ejections, which momentarily increase stellar wind densities and velocities. Figure 3 shows other exoplanets, such as GJ 674 b, GJ 876 b and YZ Cet b, that present good prospects for radio detection, provided that their quiescent wind have $\dot{M}u_{\text{sw}}^3 \gtrsim 1.8 \times 10^{-4}$.

Given that the radio flux is sensitive to the local density

and velocity of the stellar wind, we might not be able to decouple these two quantities without additional hypotheses (or additional observations), but certainly this would bring us one step closer to observationally constraining the winds of M dwarf stars. And once more exoplanets could be useful ‘wind-ometers’, i.e., tools to probe winds of their host stars (Vidotto & Bourrier 2017).

ACKNOWLEDGEMENTS

AAV acknowledges funding from the Irish Research Council Consolidator Laureate Award 2018 and thanks Dr Blakesley Burkhart for promptly clarifying details of their models. This research has made use of the NASA Exoplanet Archive, which is operated by the California Institute of Technology, under contract with the National Aeronautics and Space Administration under the Exoplanet Exploration Program. We thank the anonymous reviewer for their constructive comments.

REFERENCES

- Aitta A., 2018, arXiv e-prints, [p. arXiv:1811.09198](https://arxiv.org/abs/1811.09198)
- Alvarado-Gómez J. D., Hussain G. A. J., Cohen O., Drake J. J., Garraffo C., Grunhut J., Gombosi T. I., 2016, *A&A*, **594**, A95
- Bastian T. S., Dulk G. A., Leblanc Y., 2000, *ApJ*, **545**, 1058
- Boro Saikia S., et al., 2016, *A&A*, **594**, A29
- Burkhart B., Loeb A., 2017, *ApJ*, **849**, L10
- Chapman S., Ferraro V. C. A., 1930, *Nature*, **126**, 129
- Christensen U. R., Holzwarth V., Reiners A., 2009, *Nature*, **457**, 167
- Cloutier R., et al., 2018, *AJ*, **155**, 93
- Cravens T. E., 2004, *Physics of Solar System Plasmas*
- Davenport J. R. A., et al., 2014, *ApJ*, **797**, 122
- Davenport J. R. A., Kipping D. M., Sasselov D., Matthews J. M., Cameron C., 2016, *ApJ*, **829**, L31
- Desch M. D., Kaiser M. L., 1984, NASA STI/Recon Technical Report N, **84**
- Dewdney P. E., Hall P. J., Schilizzi R. T., Lazio T. J. L. W., 2009, *IEEE Proceedings*, **97**, 1482
- Farrell W. M., Desch M. D., Zarka P., 1999, *J. Geophys. Res.*, **104**, 14025
- Finley A. J., See V., Matt S. P., 2019, arXiv e-prints, [p. arXiv:1903.09871](https://arxiv.org/abs/1903.09871)
- Gallagher P. T., Lawrence G. R., Dennis B. R., 2003, *ApJ*, **588**, L53
- Gallet F., Bouvier J., 2015, *A&A*, **577**, A98
- Garraffo C., Drake J. J., Cohen O., 2016, *ApJ*, **833**, L4
- Gastine T., Duarte L., Wicht J., 2012, *A&A*, **546**, A19
- Griessmeier J.-M., 2017, *Planetary Radio Emissions VIII*, pp 285–299
- Griessmeier J.-M., Motschmann U., Mann G., Rucker H. O., 2005, *A&A*, **437**, 717
- Griessmeier J.-M., Zarka P., Spreeuw H., 2007, *A&A*, **475**, 359
- Griessmeier J.-M., Zarka P., Girard J. N., 2011, *Radio Science*, **46**, 0
- Hallinan G., et al., 2015, *Nature*, **523**, 568
- Hill T. W., 2001, *J. Geophys. Res.*, **106**, 8101
- Irwin J., Berta Z. K., Burke C. J., Charbonneau D., Nutzman P., West A. A., Falco E. E., 2011, *ApJ*, **727**, 56
- Jardine M., Collier Cameron A., 2019, *MNRAS*, **482**, 2853
- Johnstone C. P., Guedel M., Brott I., Lüftinger T., 2015, *A&A*, **577**, A28
- Kasting J. F., Whitmire D. P., Reynolds R. T., 1993, *Icarus*, **101**, 108
- Kavanagh R. D., et al., 2019, *MNRAS*, **485**, 4529
- Kay C., Opher M., Kornbleuth M., 2016, *ApJ*, **826**, 195
- Khodachenko M. L., et al., 2007, *Astrobiology*, **7**, 167
- Kislyakova K. G., Holmström M., Lammer H., Odert P., Khodachenko M. L., 2014, *Science*, **346**, 981
- Lammer H., et al., 2007, *Astrobiology*, **7**, 185
- Lazio T. J. W., Farrell W. M., Dietrick J., Greenlees E., Hogan E., Jones C., Hennig L. A., 2004, *ApJ*, **612**, 511
- Lazio T. J. W., et al., 2011, *Advances in Space Research*, **48**, 1942
- Llama J., Wood K., Jardine M., Vidotto A. A., Helling C., Fossati L., Haswell C. A., 2011, *MNRAS*, **416**, L41
- Llama J., Vidotto A. A., Jardine M., Wood K., Fares R., Gombosi T. I., 2013, *MNRAS*, **436**, 2179
- Matt S. P., Brun A. S., Baraffe I., Bouvier J., Chabrier G., 2015, *ApJ*, **799**, L23
- McIntyre S. R. N., Lineweaver C. H., Ireland M. J., 2019, *MNRAS*, **485**, 3999
- Mengel M. W., et al., 2016, *MNRAS*, **459**, 4325
- Nicholson B. A., et al., 2016, *MNRAS*, **459**, 1907
- O Fionnagain D., Vidotto A. A., 2018, *MNRAS*, **476**, 2465
- Ó Fionnagáin D., et al., 2019, *MNRAS*, **483**, 873
- Osten R. A., Wolk S. J., 2015, *ApJ*, **809**, 79
- Parker E. N., 1958, *ApJ*, **128**, 664
- Pasinetti Fracassini L. E., Pastori L., Covino S., Pozzi A., 2001, *A&A*, **367**, 521
- Pinto R. F., Brun A. S., Jouve L., Grappin R., 2011, *ApJ*, **737**, 72
- Quirrenbach A., et al., 2014, in *Ground-based and Airborne Instrumentation for Astronomy V*. p. 91471F, [doi:10.1117/12.2056453](https://doi.org/10.1117/12.2056453)
- Scalo J., et al., 2007, *Astrobiology*, **7**, 85
- Seager S., Kuchner M., Hier-Majumder C. A., Militzer B., 2007, *ApJ*, **669**, 1279
- See V., Jardine M., Vidotto A. A., Petit P., Marsden S. C., Jeffers S. V., do Nascimento J. D., 2014, *A&A*, **570**, A99
- See V., et al., 2016, *MNRAS*, **462**, 4442
- Siscoe G. L., Chen C.-K., 1975, *J. Geophys. Res.*, **80**, 4675
- Sullivan P. W., et al., 2015, *ApJ*, **809**, 77
- Tarduno J. A., et al., 2010, *Science*, **327**, 1238
- Varela J., Réville V., Brun A. S., Zarka P., Pantellini F., 2018, *A&A*, **616**, A182
- Vida K., et al., 2016, *A&A*, **590**, A11
- Vida K., Kóvári Z., Pál A., Oláh K., Kriskovics L., 2017, *ApJ*, **841**, 124
- Vidotto A. A., Bourrier V., 2017, *MNRAS*, **470**, 4026
- Vidotto A. A., Donati J.-F., 2017, *A&A*, **602**, A39
- Vidotto A. A., Opher M., Jatenco-Pereira V., Gombosi T. I., 2010a, *ApJ*, **720**, 1262
- Vidotto A. A., Jardine M., Helling C., 2010b, *ApJ*, **722**, L168
- Vidotto A. A., Llama J., Jardine M., Helling C., Wood K., 2011a, *Astronomische Nachrichten*, **332**, 1055
- Vidotto A. A., Jardine M., Opher M., Donati J. F., Gombosi T. I., 2011b, *MNRAS*, **412**, 351
- Vidotto A. A., Jardine M., Helling C., 2011c, *MNRAS*, **414**, 1573
- Vidotto A. A., Fares R., Jardine M., Donati J.-F., Opher M., Moutou C., Catala C., Gombosi T. I., 2012, *MNRAS*, **423**, 3285
- Vidotto A. A., Jardine M., Morin J., Donati J.-F., Lang P., Russell A. J. B., 2013, *A&A*, **557**, A67
- Vidotto A. A., Jardine M., Morin J., Donati J. F., Opher M., Gombosi T. I., 2014, *MNRAS*, **438**, 1162
- Vidotto A. A., Bisikalo D. V., Fossati L., Llama J., 2015a, in Lammer H., Khodachenko M., eds, *Astrophysics and Space Science Library Vol. 411*, Astrophysics and Space Science Library. p. 153, [doi:10.1007/978-3-319-09749-7_8](https://doi.org/10.1007/978-3-319-09749-7_8)

- Vidotto A. A., Fares R., Jardine M., Moutou C., Donati J.-F., 2015b, [MNRAS](#), **449**, 4117
- Villarreal D'Angelo C., Jardine M., See V., 2018, [MNRAS](#), **475**, L25
- Weber C., et al., 2017, [MNRAS](#), **469**, 3505
- West A. A., Hawley S. L., Bochanski J. J., Covey K. R., Reid I. N., Dhital S., Hilton E. J., Masuda M., 2008, [AJ](#), **135**, 785
- Wood B. E., 2004, *Living Reviews in Solar Physics*, **1**, 2
- Wood B. E., Linsky J. L., Müller H., Zank G. P., 2001, [ApJ](#), **547**, L49
- Wood B. E., Müller H.-R., Zank G. P., Linsky J. L., Redfield S., 2005, [ApJ](#), **628**, L143
- Wu C. S., Lee L. C., 1979, [ApJ](#), **230**, 621
- Zarka P., 2007, [Planet. Space Sci.](#), **55**, 598
- Zarka P., Cecconi B., Kurth W. S., 2004, [J. Geophys. Res. \(Space Physics\)](#), **109**, 9
- Zarka P., et al., 2012, [Planet. Space Sci.](#), **74**, 156
- Zuluaga J. I., Bustamante S., 2016, arXiv e-prints,
- Zuluaga J. I., Cuartas P. A., 2012, [Icarus](#), **217**, 88
- de Gasperin F., et al., 2019, [A&A](#), **622**, A5

This paper has been typeset from a $\text{\TeX}/\text{\LaTeX}$ file prepared by the author.